NASA Technical Memorandum 81209

Shape Change of Galileo Probe Models in Free-Flight Tests

Chul Park and Charles E. De Rose

June 1980

NASA
National Aeronautics and
Space Administration

NASA Technical Memorandum 81209

Shape Change of Galileo Probe Models in Free-Flight Tests

Chul Park
Charles E. De Rose, Ames Research Center, Moffett Field, California

NASA
National Aeronautics and
Space Administration

Ames Research Center
Moffett Field, California 94035

SHAPE CHANGE OF GALILEO PROBE MODELS IN FREE-FLIGHT TESTS

Chul Park and Charles E. De Rose

Ames Research Center

SUMMARY

Scale models of the Galileo Probe made of polycarbonate, AXF5Q graphite, carbon-carbon composite, and carbon-phenolic were flown in a free-flight range in an ambient gas of air, krypton, or xenon. Mach numbers varied between 14 and 24, Reynolds numbers between 3×10^5 and 10×10^5, stagnation pressures between 31 and 200 atm, and stagnation-point heat-transfer rates between 10 and 1,000 kW/cm^2. Shadowgraphs indicate gouging ablation of the aft portion of the frustum; the gouging was moderate in air and severe in the noble gases. The graphite models break in the same region. An explanation of the phenomena is offered in terms of the strong compression and shear caused by the reattachment of a turbulent separated flow. Conditions are calculated for similar tests appropriate for Von Karman Facility of the AEDC in which a larger model can be flown in argon.

INTRODUCTION

The problem of ablation of the heat shield for Galileo Probe, the spacecraft designed to enter the atmosphere of Jupiter, has been studied in some depth in recent years. One aspect of the problem yet unresolved is the question of shape change of the heat shield during the entry flight. The high heating rates predicted during the flight are expected to cause ablation of the heat shield to such an extent that the geometry of the shield will be changed substantially. If the shape of the heat shield changes in a way different from that predicted, the locally high heat-transfer rates caused by the shape change might cause the shield to fail.

It is generally agreed that appreciable shape change will occur at the stagnation point due to the high heat-transfer rates there (see, e.g., ref. 1). Nicolet et al. (ref. 2) predict also that rapid ablation might occur at a point away from the stagnation point, leading to change of shape; this change of shape will be termed "gouging" in the present work. The predicted gouging phenomenon is believed to be associated with turbulence which can cause an increase in both convective and radiative heat-transfer rates (ref. 2).

Such theoretical predictions must be regarded as speculative. Certainly, the location of the laminar-to-turbulent transition is unknown. Under the premise that the most pessimistic and hence conservative prediction will result if the transition is assumed to occur early, Nicolet et al. assumed the transition to occur at points infinitesimally close to the stagnation point (ref. 2). This led them to conclude that the gouging ablation will occur at points close to the stagnation point.

The purpose of the present work is to search experimentally for clues about gouging ablation — whether it occurs and where. For this purpose, scale models of Galileo Probe were flown in a free-flight range. By maintaining the flight Mach numbers above 14, the hypersonic features of the Jovian entry flights were reproduced. The Reynolds numbers were varied to cover the peak heating conditions during the Jovian flight. Large radiative heat-transfer rates were produced by passing the models through a noble gas (krypton or xenon); radiative heat fluxes of over 1,000 kW/cm^2 were produced at the stagnation point by this means. Changes in the shapes of the models were observed with shadowgraph cameras.

The results show that gouging ablation does indeed occur, but mostly in the aft portion of the frustum. This result confirms the occurrence of the gouging ablation predicted by Nicolet et al. (ref. 2) but contradicts its location. The possible causes and consequences of this phenomenon are discussed. Finally, a calculation is performed for the conditions and environments of a large model flying through argon, as would be appropriate for tests in a large free-flight range at AEDC.

EXPERIMENTAL TECHNIQUES

Scale models of Galileo Probe were made of polycarbonate (trade name Lexan), AXF5Q graphite made by Poco Graphite, Inc., reinforced carbon-carbon composite, and carbon-phenolic. The diameter of the frustum of the polycarbonate model was 2.5 cm; the diameter of the other models was 1.905 cm (fig. 1). The afterbody shape of the polycarbonate models deviated from that of the Galileo Probe as shown.

The experiments were conducted in a free-flight range facility at Ames Research Center (fig. 2). The models were launched with a light-gas gun having a launch-tube diameter of 2.54 cm. The scale models shown in figure 1(b) were launched in a sabot; polycarbonate models (fig. 1(a)) were launched directly without the sabot. The range was filled with air at 100 Torr. Aerodynamic forces cause the sabot to separate before the model reached the baffle, and the model proceeded through the opening at the center of the baffle. Seven shadowgraph observation stations were located at intervals of 1.52 m along the length of the test facility, starting at a distance of 10 m downstream of the muzzle of the gun.

A chamber, filled with either krypton (at 100 or 200 Torr) or xenon (at 100 Torr), was located between stations 1 and 3 (fig. 1). Mylar diaphragms were used to seal the ends of the chamber — the upstream diaphragm was transparent and 0.0127 mm thick; the downstream diaphragm was opaque and 0.127 mm thick. The thick, opaque downstream diaphragm was necessary to minimize the precursor phenomenon to be described below. Three regions are defined in the test facility: region 1 is the air region in front of the noble gas chamber; region 2 is the noble gas region; and region 3 is the air region beyond the noble gas chamber.

The shadowgraph cameras were equipped with Kerr cell shutters with open durations of 40 nsec. The shutters were opened normally by a pulse signal generated by a photoelectric sensor located at each observation station. The sensors viewed the centerline of the range to receive the beam of light originating in a tungsten filament lamp. When the model arrived at the center of the observing field, the beam of light was intercepted. This caused a reduction in the electric current through the sensor, which in turn produced the pulse that triggered the Kerr cell shutter. The absolute magnitude of the rate of change of the electric current must be greater than a certain minimum value for a successful triggering.

At station 1, the Kerr cell shutter opened without difficulty. At stations 2 and 3, there was a tendency for the trigger pulses to be generated prematurely or not at all; this trend was particularly severe at station 2. By monitoring the current through the sensors, it was found that the ambient gas emits radiation nearly 50 μsec prior to the arrival of the model. The strongest luminosity, generated by the models flying through xenon, was greater than that of the tungsten lamp by at least 6 orders of magnitude. The electric current produced by the gas luminosity varied so gradually with time that it frequently failed to produce the triggering pulse. The Kerr cell shutter for station 2 was opened, therefore, by the pulse generated externally after a fixed delay time after the pulse at station 1 was generated. This method relied on the reproducibility of the launch speed. Since the launch speed could not be reproduced accurately, the Kerr cell shutter at station 2 failed occasionally to open at the required instant. Station 3 tended to trigger prematurely; this tendency was lessened somewhat by using the opaque diaphragm mentioned earlier.

At station 2, only one shadowgraph camera was installed. Elsewhere, two cameras were installed at each station, one through a horizontal optical axis (identified as the "side" position) and the other through a vertical axis ("top" position).

TEST ENVIRONMENTS

The basic launch conditions of the tests are summarized in table 1. The velocities at the muzzle and the average velocity in region 1 are calculated by extrapolating the downstream velocity values. From the rates of velocity decay observed in regions 2 and 3, one can determine the effective ballistic coefficients. The upstream velocities were calculated assuming that the ballistic coefficients remained the same throughout each flight. The flow Mach numbers for regions 1 and 2 are listed in table 2. Although the Mach numbers are smaller than the Mach 50 value in the Jovian flight, the hypersonic features of the flow are believed to be adequately simulated by the present tests.

In the Jovian entry flight, the Reynolds number based on the free-stream condition and the nose radius is predicted to reach a maximum of about 8×10^5. Since the Jovian atmosphere is cold (about 150 K), the Reynolds number value

is biased toward the cold ambient temperature. Physically, the viscous phenomena in the shock layer are affected mostly by the wall temperature, which would be about the same on the Jovian flight as in the present tests. To make a fair comparison between the Reynolds numbers of the present tests and those of the Jovian flight, therefore, the Reynolds numbers of the tests are extrapolated to the hypothetical free-stream temperature of 150 K by using the viscosity value at 150 K. As seen in the table, the Jovian-equivalent Reynolds numbers of the present tests cover the peak value of the Jovian entry flight.

The shock layer flows in regions 1 and 3 are in a dissociating regime. The convective heat-transfer rates to the stagnation point are calculated for region 1 with the formula of Fay and Riddell (ref. 3); they are presented in table 2.

In region 2, temperatures in the shock layer are approximately 20,000 K. The flow is in an ionizing regime, as indicated in table 3; a strong radiation is likely to occur in this region. The "unblocked" radiative heat fluxes, that is, the heat flux values calculated assuming an inviscid flow, which are believed to equal approximately the heat flux values at the interface between the inviscid shock layer and the ablation-product layer, were calculated in the present study at the stagnation point as follows.

To calculate the unblocked radiative heat flux, one must account for the radiative cooling. Along the stagnation streamline, the cooling effect is calculated by solving the energy equation

$$\rho v \frac{\partial H}{\partial y} = - \frac{\partial q}{\partial y}$$

where ρ, v, H, and q are density, normal velocity, total enthalpy, and radiative heat flux, respectively, and y is the normal coordinate. The solution was obtained by assuming ρv to be proportional to y. The heat flux q was calculated through iteration using a modified version of the computer code ARCRAP (ref. 4). The shock layer was divided into six isothermal layers, and the radiation calculation was carried out line by line as in reference 4. Iteration was continued until a consistent set of temperature and heat flux values was found.

To verify the accuracy of the present procedure for computing the radiative heat fluxes, the code was applied to a known solution. The unpublished solution obtained previously by Moss of Langley Research Center for the 89% hydrogen-11% helium atmosphere at a flight velocity of 41.2 km/sec and a stagnation pressure of 5.1 atm was selected as the test case. The original solution of Moss resulted in the interface heat flux of 48.6 kW/cm^2. Arnold et al. (ref. 4) repeated the radiative heat flux calculation line by line using 18 isothermal layers and obtained an interface heat flux of 56.45 kW/cm^2. The present simplified code resulted in 56.67 kW/cm^2. The agreement between the present 6-layer model and the 18-layer model of Arnold et al. is attributable partly to the fact that the two codes use the same spectroscopic subroutine package. In any case, accuracy of the present code was judged sufficient for the present study.

To carry out the calculation for krypton and xenon, spectroscopic data for these gases must be provided. There are numerous theoretical and experimental data on line transition probabilities for krypton and xenon, which are reviewed in reference 5. Stark widths of a few prominent lines of these two gases are known; they are reviewed in references 6-9. After a careful comparison of these data, the values presented in tables 4 and 5 are adopted for the transition probability and the Stark width. For the lines for which the Stark widths are not known, the semiempirical formula used by Arnold et al. (ref. 4) was used. Numerous theoretical and experimental data exist also for continua of krypton and xenon (ref. 5). After screening these data, the theoretical values of Schlüter (refs. 10, 11), were selected for use in the present work for the wavelength range of 2,000 Å to 30,000 Å. For the wavelength range below 2,000 Å, the data of Samson and Kelly (ref. 12) were used. For the regime of wavelengths greater than 30,000 Å, the continua of krypton and xenon were assumed to be the same as for atomic hydrogen.

Typical spectra of radiation incident on the stagnation point are shown in figure 3; the heat flux values are listed in table 2. As seen in figure 3, spectra produced in the present tests are nearly continuous. The figure also shows the locations of the bands of C_3, C_2, and CO, which could absorb the incident radiation. Since the incident radiation is nearly continuous, the probability of absorption by these bands is high. One expects, therefore, that the blockage by the ablation-product layer in the present tests was more effective than in the Jovian flight.

Using the heat flux values of table 2, the temperature distribution within the model at the stagnation point is calculated. The one-dimensional unsteady heat conduction equation for variable conductivity and variable specific heat was solved numerically for this purpose. The conductivity and specific heat values for the four materials were obtained from the existing unpublished sources. For carbon-phenolic, which undergoes charring, the values for virgin material were used in the calculation in the belief that the charring phenomenon is not predominant in the present environments.

Figure 4 shows temperature distribution at three different instances for two models. As seen here, heat penetrates much less than 1 mm at the stagnation point. Figure 5 shows the history of the stagnation point surface temperature for four tests. The temperature and electron density values for the four tests are presented in table 3. As seen in figure 5, the wall temperature of polycarbonate reaches the assumed vaporization temperature of 1,000 K early in region 1. The exact vaporization temperature of polycarbonate is unknown because of its glassy nature. For the graphite, carbon-carbon and carbon-phenolic vaporization point is reached almost instantly (to within 10 μsec) as the model enters region 2.

From these heat flux values, the stagnation-point recessions expected at station 3 were calculated for the three graphitic materials; they are presented in table 2. The recession values are obtained by assuming the radiative blockage to be 0.5 and the effective heat of sublimation to be 27 kJ/g. As seen in the table, the recessions are less than 0.1 mm, which would be too small to be detected by the shadowgraph method used.

RESULTS

Shadowgraphs obtained in the tests are presented in figures 6 through 16. A microphotodensitometer trace of a shadowgraph is presented in figure 17. In presenting the data, one photograph was selected from each of regions 1 and 3. Region 1, consisting of station 1, produced two shadowgraphs (top and side positions) and region 3 produced up to 12 (top and side positions at six different locations). Only the clearest of these shadowgraphs are presented here in order to limit the size of this report. As mentioned in Experimental Techniques, there was only one camera at station 2, and it yielded a successful picture only when the launch speed matched the external time delay setting.

In examining the photographs, one common feature stands out clearly: all runs indicate a severe environment (i.e., large heat-transfer rate or shear or both) in the aft portion of the conical frustum. That is, gouging ablation takes place in the aft region. This single observation is elaborated as follows:

1. Polycarbonate tests, runs 1536-1538. For run 1536, which had the highest launch speed, the frustum gouging is recognizable at station 1 (fig. 6(a)). At station 5, all three runs show signs of frustum gouging. The two shadowgraphs taken at station 2 show the bright region in the aft portion of the shock layer. The bright region is believed to be due to a steep shock angle caused by the gouging.

2. AXF5Q graphite tests, runs 1539-1543. The models broke in all these runs, but the manner in which they broke shows that the most severe stress occurred in the aft portion of the frustum. In particular, for run 1539, the model was intact in region 1. In region 2, the model lost its frustum edge. The picture at station 5 shows the model breaking in the frustum region. In run 1540, the frustum gouging occurred in region 1. In region 2, the frustum edge broke away as in run 1539. In runs 1541 and 1542, the aft portion of the frustum broke away before the model reached station 1, and in run 1543, the frustum was gouged before the model reached station 1.

3. Carbon-carbon test, run 1544. There is a sign of frustum gouging in the photograph taken at station 1. At station 5, the gouging phenomenon is clearer. In the photograph taken at station 2, the bright region exists near the frustum edge, as was the case in the previous runs. One notes here that the photographs from stations 2 and 5 show signs of rough surfaces. One can attribute this to the fact that carbon-carbon composite has a quilted, woven structure. The graphitic fibers can resist the shear and internal vapor pressure much more than the filler; as a result, filler material is lost before the fibers are lost. The relative scale of the weave mesh to the body size is relatively large here, and is certainly much larger than in the prototype. Nevertheless, the region of gouging seems to be almost at the same location as for other models.

4. Carbon-phenolic tests, runs 1545 and 1546. In these tests, one sees a faint sign of frustum gouging in the photographs taken at station 1. In

the photographs taken at stations 2 and 7, these signs are unmistakable. The densitograph scan of figure 16(c), shown in figure 17, confirms the existence of the bright region in the shock layer near the frustum edge. Gouging of this material is particularly interesting because this is the material that will be used on the Galileo Probe. The depths of the gougings shown in figures 15(b) and 16(b) are about 0.5 mm.

Another interesting feature in the shadowgraphs is the presence of a dark trail in the afterbody region for all tests except those with the ATJS graphite models. The dark region signifies attenuation of radiation from the shadowgraph light source and can be due only to particulates. If the dark regions were due to gases, the afterbody region would be more luminous than the free stream because a gas of high opacity should be radiating at the temperatures expected in the region. Temperatures in the afterbody region are expected to be high (i.e., between 15,000 and 20,000 K in noble gases) if the region is free of solid particulates.

In the case of polycarbonate models, the presence of particulates is expected. The vaporization temperature of the material is lower than the temperature at which solid carbon can exist. The ablation product vapor could undergo chemical reactions and pyrolysis to form solid carbon. Presence of particulates in the tests with carbon-carbon and carbon-phenolic models can be attributed to spallation. It is impossible for the particulates to be produced by condensation of originally gaseous species. The high temperature in the region would prohibit such condensation; nor would there be any means of removing the heat of condensation. Spallation of graphitic materials has been observed in arc-jet tests (ref. 13), and the observed spallation of the two graphitic materials is not surprising for the conditions of the present tests.

The fact that the graphite models show no signs of spallation is quite surprising, however. Since the graphite is similar to carbon-carbon composite in chemical composition, it is unlikely that the graphite would behave so much differently from carbon-carbon. It is more likely that the cause of the difference is something else; for instance, it is possible that the apparent spallation in the two graphitic materials occurs over the aft portion of the frustum where the apparent gouging occurs. The graphite models lose the aft portion before they reach station 2, and therefore cannot exhibit the spallation phenomenon.

DISCUSSION

As mentioned earlier, the depth of gouging in the aft portion of the frustum is about 0.5 mm for the carbon-phenolic models, which is an order of magnitude greater than the maximum possible recession expected at the stagnation point. Since the stagnation point shows no discernible recession, one must conclude that the gouged region is subject to a stress environment more severe than that at the stagnation point.

It is interesting to compare the present results with those of an earlier test made with a steel model (ref 14). In that test, the ambient conditions and launch velocity were such that the heat-transfer rate and stagnation point pressure were about twice those of region 1 in the present tests, but the duration of the observed flight was much longer. Considering the fact that gouging was observed at the end of region 1 in the present tests, one would expect to see the same in the steel model. But there was no sign of gouging ablation in the test with the steel model. This fact seems to indicate that the gouging phenomenon is related to the mechanical strength and thermal conductivity of the material. The materials used in the present tests have mechanical strengths and conductivity values much smaller than those of steel. It is believed that a low thermal conductivity causes a strong thermal stress to develop in the immediate vicinity of the surface, and if the tensile-compression strength of the material is not high enough to withstand the stress, the material can fail mechanically (ref. 15).

A large heat-transfer rate and a strong shear could develop over the observed gouged region if the boundary-layer flow underwent separation in the upstream and reattached at the region. At the juncture of the hemisphere and the cone, the pressure gradient approaches zero or even becomes positive (ref. 16). Boundary-layer flow could spearate in this region, as illustrated schematically in figure 18(a). The separated flow can reattach over the downstream portion of the frustum, as shown. Convective heat-transfer rate and skin friction would become large at this point because the normal velocity gradient would be large. Radiative heat-transfer rate could increase also if an embedded shock wave were to form here. The resulting ablation pattern would be the one shown schematically in figure 18(b).

Howe (ref. 15) calculates that a heat-transfer rate of a few kilowatts per square centimeter could produce a compression stress of the order of 100 kg/cm^2. In the present tests, the heat-transfer values were much larger. Because such a stress would be concentrated at the reattachment point, a failure is likely to occur. The failure could be in the form of spallation, as Howe (ref. 15) predicts, or of a more drastic nature, such as that seen with the AXF5Q models. If the flow is turbulent prior to separation, the skin friction at the reattachment point would be equal approximately to ρu^2, which will be about 50 kg/cm^2 in region 1 and 100 to 200 kg/cm^2 in region 2. Such stress will contribute further toward mechanical failure.

The gouging phenomenon observed here confirms qualitatively the prediction of Nicolet et al. (ref. 2). Quantitatively, however, the location of the gouging is found to be much farther downstream of that predicted by Nicolet et al. Moreover, the observed phenomenon is a more serious problem than they predicted, not only because the area affected is larger in the aft portion, but because the added heat shield weight in the aft region will shift the center of gravity backward and therefore tend to make the spacecraft aerodynamically less stable.

The fact that the observed gouging occurs at about the same location for all four materials and at all Reynolds numbers tested leads one to believe that the phenomenon is due to reattachment of a separated flow in a flow that is originally turbulent. The surface structures of the four materials are

considerably different. Polycarbonate is glassy at elevated temperatures and melts at a temperature below 1,000 K; hence, its surface must have been microscopically smooth over the entire body. Carbon-carbon composite produces a rough surface, as evidenced in figures 14(b) and 14(c). If the boundary-layer flow was turbulent before the flow separated, the geometry of separated flow will be independent of the transition point. The flight Reynolds numbers (i.e., those based on the nose radius) were high enough to cause turbulent transition over the hemispherical nose region.

Because of the potential seriousness of the gouging problem in relation to the Galileo Probe, it would seem desirable to repeat the present experiment using a different facility and in environments that more closely simulate the Jovian flight conditions. Also, it would be highly desirable to recover the model after the flight. Such tests can be made, for instance, using the Range G of the Von Karman Facility of the AEDC. Calculations were made for such tests assuming (1) a model nose radius of 1.5 cm, (2) ambient gas of argon, and (3) a constant speed flight over 250 m. The transition probability and Stark-width values necessary for the calculation were taken from references 17 and 18. A total of 97 lines were included in the calculation. Continuum intensities were obtained from references 10, 11, and 19.

Figure 19 shows the calculated radiative heat flux values at the stagnation point of the inviscid shock layer. The Jovian flight value of 56.7 kW/cm^2 shown in the figure is that computed by the present computer code. As the figure shows, radiative heat flux of the Jovian entry condition can be reproduced easily in such tests at modest velocities of 4 to 5 km/sec.

Figure 20 shows a typical calculated spectrum of the radiation. As seen here, the spectrum is almost continuous. The locations of the absorption bands of C_3, C_2, and CO are shown also. As mentioned earlier, the blockage by the ablation product layer in such tests would be more efficient than in the Jovian entry flight. In order to produce the same wall heat flux as in the Jovian flight case, therefore, the inviscid radiation flux must be made higher in the tests than that in the Jovian flight.

Table 6 lists two such possible test conditions. As seen in the table, Reynolds numbers and heat fluxes can be matched simultaneously with the Jovian flight values. Stagnation pressure is only about a factor of 5 higher than in the Jovian flight. The table also lists the stagnation-point recession values calculated assuming a blockage factor of 0.5 and a sublimation energy of 27 kJ/g. As seen in the table, the recession will be large enough to be measurable by shadowgraph. An effort is currently being made at Ames Research Center to carry out such tests.

CONCLUSIONS

Free-flight tests made with scale models of Galileo Probe at realistic Mach and Reynolds numbers indicate that severe heating or shear or both occur over the aft portion of the conical frustum. Polycarbonate, AXF5Q graphite, reinforced carbon-carbon composite, and carbon-phenolic models all exhibit

gouging ablation in their aft regions to depths much larger than possible at the stagnation point. Luminosity of the shock layer is high over the region because of the steep shock angle caused by the gouging. Polycarbonate, carbon-carbon, and carbon-phenolic produce spallation, apparently at the region of gouging, and the graphite models break at the same region. The phenomena can be attributed to reattachment of a turbulent separated flow. Further experimental verification of the observed phenomena can be made with advantage in a large facility using argon as the test gas.

REFERENCES

1. Dirling, R. B.; and Binder, J. D.: Jupiter Probe Heat-Shield Configuration Optimization. Outer Planet Entry Heating and Thermal Protection, Progress in Astronautics and Aeronautics, Vol. 64, R. Viskanta, ed., American Institute of Aeronautics and Astronautics, New York, N.Y., 1979, pp. 321-344.

2. Nicolet, W. E.; Davy, W. C.; and Wilson, J. F.: Galileo Probe Forebody Entry Thermal Protection: Aerothermal Environments and Heat Shielding Requirements. Paper 80-ENAS-24 ASME/SAE/AICHE/AIAA/ASMA 10th Intersociety Conference on Environmental Systems, San Diego, Calif., July 1980.

3. Fay, J. A.; and Riddell, F. R.: Theory of Stagnation Point Heat Transfer in Dissociated Air. J. Aeronaut. Sci., vol. 25, no. 2, Feb. 1958, pp. 73-85.

4. Arnold, J. O.; Cooper, D. M.; Park, C.; and Prakash, S. G.: Line-by-Line Transport Calculations for Jupiter Entry Probes. AIAA Paper 79-1082, AIAA 14th Thermophysics Conference, Orlando, Fla., June 1979.

5. Fuhr, J. R.; Miller, B. J.; and Martin, G. A.: Bibliography on Atomic Transition Probabilities (1914 through October 1977). National Bureau of Standards Special Publication 505, U.S. Department of Commerce, Washington, D.C., Apr. 1978.

6. Fuhr, J. W.; Wiese, W. L.; and Roszman, L. J.: Bibliography on Atomic Line Shapes and Shifts (1889 through March 1972). National Bureau of Standards Special Publication 336, U.S. Department of Commerce, Washington, D.C., Sept. 1972.

7. Fuhr, J. W.; Wiese, W. L.; and Roszman, L. J.: Bibliography on Atomic Line Shapes and Shifts (April 1972 through June 1973). Supplement 1, National Bureau of Standards Special Publication 336, U.S. Department of Commerce, Washington, D.C., Nov. 1973.

8. Fuhr, J. W.; Wiese, W. L.; and Roszman, L. J.: Bibliography on Atomic Line Shapes and Shifts (July 1973 through May 1975). Supplement 2, National Bureau of Standards Special Publication 336, U.S. Department of Commerce, Washington D.C., Nov. 1975.

9. Fuhr, J. W.; Wiese, W. L.; and Roszman, L. J.: Bibliography on Atomic Line Shapes and Shifts (July 1975 through June 1978). Supplement 3, National Bureau of Standards Special Publication 336, U.S. Department of Commerce, Washington, D.C., Dec. 1978.

10. Schlüter, D.: Die Berechnung der Übergangswahrscheinlichkeiten von Seriengrenzkontinua mit Anwendung auf die schweren Edelgase. Z. Astrophys., vol. 61, no. 1, Mar. 1965, pp. 67-76.

11. Schlüter, D.: Die Emissionskontinua thermischer Edelgasplasmen. Z. Phys., vol. 210, no. 1, Feb. 1968, pp. 80-91.

12. Samson, J. A. R.; and Kelly, F. L.: Planetary Physics III: Photoionization Cross Sections of the Rare Gases. Technical Report 64-3-N, Geophysics Corporation of America, Bedford, Mass., Jan. 1964.

13. Lundell, J. H.; and Dickey, R. R.: Ablation of ATJ Graphite at High Temperatures. AIAA Journal, vol. 11, no. 2, Feb. 1973, pp. 216-222.

14. Park, C.: Modeling of Radiative Heating of Base Region of Jovian Entry Probe. AIAA Paper 79-0039, 17th Aerospace Sciences Meeting, New Orleans, La., Jan. 1979.

15. Howe, J. T.: Thermal-Mechanical Response of Nearly Opaque Materials Exposed to Continuous Radiation. AIAA Journal, vol. 9, no. 10, Oct. 1971, pp. 1911-1920.

16. Lombard, C. K.; Davy, W. C.; and Green, M. J.: Forebody and Base Region Real Gas Flow in Severe Planetary Entry by a Factored Implicit Numerical Method — Part 1 (Computational Fluid Dynamics). AIAA Paper 80-0065, AIAA 18th Aerospace Sciences Meeting, Pasadena, Calif., Jan. 1980.

17. Wiese, W. L.; Smith, M. W.; and Miles, B. M.: Atomic Transition Probabilities, Vol. II Sodium Through Calcium. NSRDS-NBS 22, National Bureau of Standards, Washington, D.C., Oct. 1969.

18. Griem, H. R.: Plasma Spectroscopy. McGraw-Hill, New York, 1964, pp. 492-493, 523.

19. Samson, J. A. R.: Photoionization Cross Sections in Argon From Threshold to 280 Å. J. Opt. Soc. Am., vol. 54, no. 3, Mar. 1964, pp. 420-421.

TABLE 1.- AMBIENT CONDITION, MODEL AND VELOCITY DATA

Run no.	Model material	Nose radius, cm	Region 2			Velocity, km/sec		
			Gas	Press. Torr	Muzzle	Region 1 average	Region 2 average	Region 3 average
1536	Polycarbonate	0.635	Krypton	100	5.340	5.312	4.626	3.968
1537	Polycarbonate	.635			4.953	4.892	4.443	4.056
1538	Polycarbonate	.635			4.953	4.890	4.449	4.071
1539	Graphite	0.4763			5.023	4.965	4.462	4.018
1540	Graphite			200	5.084	4.953	4.305	3.790
1541	Graphite			200	4.543	4.515	3.850	3.215
1542	Graphite			200	5.269	5.216	4.520	4.250
1543	Graphite		Xenon	100	5.203	5.151	4.298	3.497
1544	Carbon-carbon				5.267	5.221	4.426	3.677
1545	Carbon-phenolic				5.119	4.997	4.143	3.413
1546	Carbon-phenolic				5.093	4.958	4.113	3.404

TABLE 2.- CALCULATED FLOW ENVIRONMENT

Run no.	Mach no.		Jovian equivalent Reynolds no.		Stagnation pressure, atm		Stagnation heat-transfer rate, kW/cm^2		Recession at sta. 3, mm
	Region 1	Region 2	Region 1	Region 2	Region 1	Region 2	Region 1 convective	Region 2 radiative	
1536	15.6	20.2	4.08×10^5	8.18×10^5	43.3	104	15.0	841	
1537	14.4	19.4	3.77	7.86	36.9	96	11.4	750	
1538	14.4	19.4	3.79	7.87	37.0	96	11.4	751	
1539	14.6	19.5	2.89	5.92	38.2	97	13.9	755	0.053
1540	14.6	18.8	2.88	1.14×10^6	38.0	180	13.7	832	0.061
1541	13.3	16.8	2.63	1.02	31.6	144	10.0	501	0.041
1542	15.3	19.8	3.05	8.93×10^5	42.4	198	16.4	1000	0.069
1543	15.2	23.5	3.01	9.80	41.3	140	15.9	1150	0.084
1544	15.4	24.	3.04	1.01×10^6	42.4	149	16.5	1260	0.089
1545	14.7	22.7	2.91	9.45×10^5	38.7	130	14.2	1040	0.078
1546	14.6	22.5	2.88	9.38	38.1	129	13.8	1000	0.076

TABLE 3.- CALCULATED TEMPERATURE AND ELECTRON DENSITY BEHIND THE SHOCK AND AT THE INNER EDGE OF THE INVISCID SHOCK LAYER AT THE STAGNATION POINT

Run No.	Behind shock		Inner edge	
	T, K	Ne, cm^{-3}	T, K	Ne, cm^{-3}
1537	20720	5.60×10^{18}	20570	5.48×10^{18}
1539	20800	5.70×10^{18}	20650	5.57×10^{18}
1544	22850	1.43×10^{19}	22650	1.40×10^{19}
1546	21510	1.15×10^{19}	21310	1.13×10^{19}

TABLE 4.- UPPER-STATE DEGENERACY g_u, TRANSITION PROBABILITY A, AND HALF-HALF STARK WIDTH AT ELECTRON DENSITY OF 10^{16} cm^{-3} w OF PROMINENT LINES OF KRYPTON

Wave-length, Å	g_u	$A \times 10^{-6}$, sec^{-1}	w, Å	Wave-length, Å	g_u	$A \times 10^{-6}$, sec^{-1}	w, Å
9751.8	3	2.63		5570.3	3	19.3	0.0480
8928.7	3	32.3		5562.2	5	3.25	
8776.7	5	23		4502.4	5	1.71	.159
8508.9	3	20.9		4463.7	3	3.66	
8298.1	3	13.6	0.0735	4453.9	5	1.23	
8281.1	3	16.44		4425.2	3	1.62	
8263.2	5	32.3		4400.0	5	3.3	
8190.1	5	5.1	.0740	4376.1	1	8.04	.210
8112.9	7	16.9	.0665	4362.6	3	1.54	
8104.4	5	68.0		4319.6	5	2.34	
8059.5	3	8.38	.0545	4318.6	5	2.34	
7928.6	5	2.92		4283.0	3	.923	
7854.8	3	10.8	.0770	4274.0	5	3.42	
7694.5	3	5.0		1235.8	3	298	
7685.2	1	22.4	.0895	1164.9	3	308	
7601.5	5	78.7	.0800	1030.0	3	300	
7587.4	1	21.9		1003.5	3	300	
5870.9	5	16.1	.0610				

TABLE 5.- UPPER-STATE DEGENERACY g_u, TRANSITION PROBABILITY A, AND HALF-HALF STARK WIDTH AT ELECTRON DENSITY OF 10^{16} cm^{-3} w OF PROMINENT LINES OF XENON

Wavelength, Å	g_u	$A \times 10^{-6}$, sec^{-1}	w, Å	Wavelength, Å	g_u	$A \times 10^{-6}$, sec^{-1}	w, Å
10838.3	3	0.97		4923.2	5	1.8	
9923.2	5	13		4916.5	3	.25	
9799.7	3	21		4843.3	5	.66	
9162.7	3	25		4829.7	3	2.1	0.238
9045.4	5	10		4807.0	1	2.6	
8952.3	5	11		4792.6	3	.51	
8930.8	3	14		4734.2	5	1.5	.0710
8819.4	7	30		4697.0	5	.74	
8409.2	3	2.1		4691.0	3	.033	
8346.8	5	35		4671.2	7	2.9	.334
8280.1	1	36		4624.3	5	2.2	
8266.5	3	14		4611.9	3	.26	
8231.6	5	23		4582.7	1	.33	
7887.4	1	42		4524.7	5	.25	
7642.0	3	28		4501.0	3	1.9	
6882.2	7	6.4		4383.9	5	.084	
6318.1	9	2.7		4193.5	7	.22	
6182.4	7	3.38		1469.6	3	234	
5695.8	5	.16		1295.6	3	258	
5028.3	3	.39					

TABLE 6.- CALCULATED ENVIRONMENTS OF FREE-FLIGHT TESTS IN ARGON ATMOSPHERE WITH A MODEL HAVING A NOSE RADIUS OF 1.5 cm

Condition	A	B
Ambient pressure, Torr	50	100
Velocity, km/sec	5.0	4.5
Mach number	15.0	13.5
R.N. = $\rho_\infty V_\infty Rn/\mu_\infty$	3.59×10^5	6.46×10^5
Jovian equivalent R.N.	5.08×10^5	9.14×10^5
After-shock T, K	17170	16062
After-shock Ne, cm^{-3}	7.92×10^{17}	7.12×10^{17}
Interface T, K	16920	15870
Interface Ne, cm^{-3}	7.34×10^{17}	6.64×10^{17}
Convective q, kW/cm^2	6.50	5.83
Radiative (unblocked) q, kW/cm^2	93.4	80.6
Stagnation pressure, atm	26.3	42.6
Recession,[a] cm	.054	.052

[a]Assumed radiation blockage = 0.5, vaporization heat = 27 kJ/g, density = 1.6 g/cm^3, range length = 250 m.

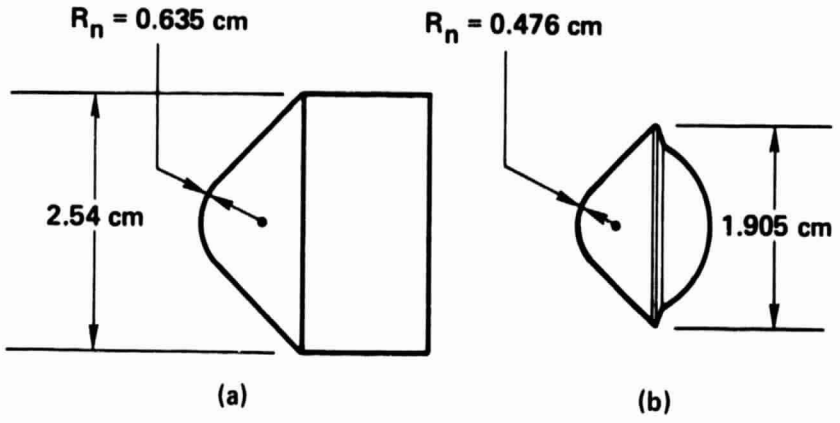

Figure 1.- Geometry of models. (a) Polycarbonate (Lexan). (b) AXF5Q graphite, carbon-carbon composite, and carbon-phenolic models.

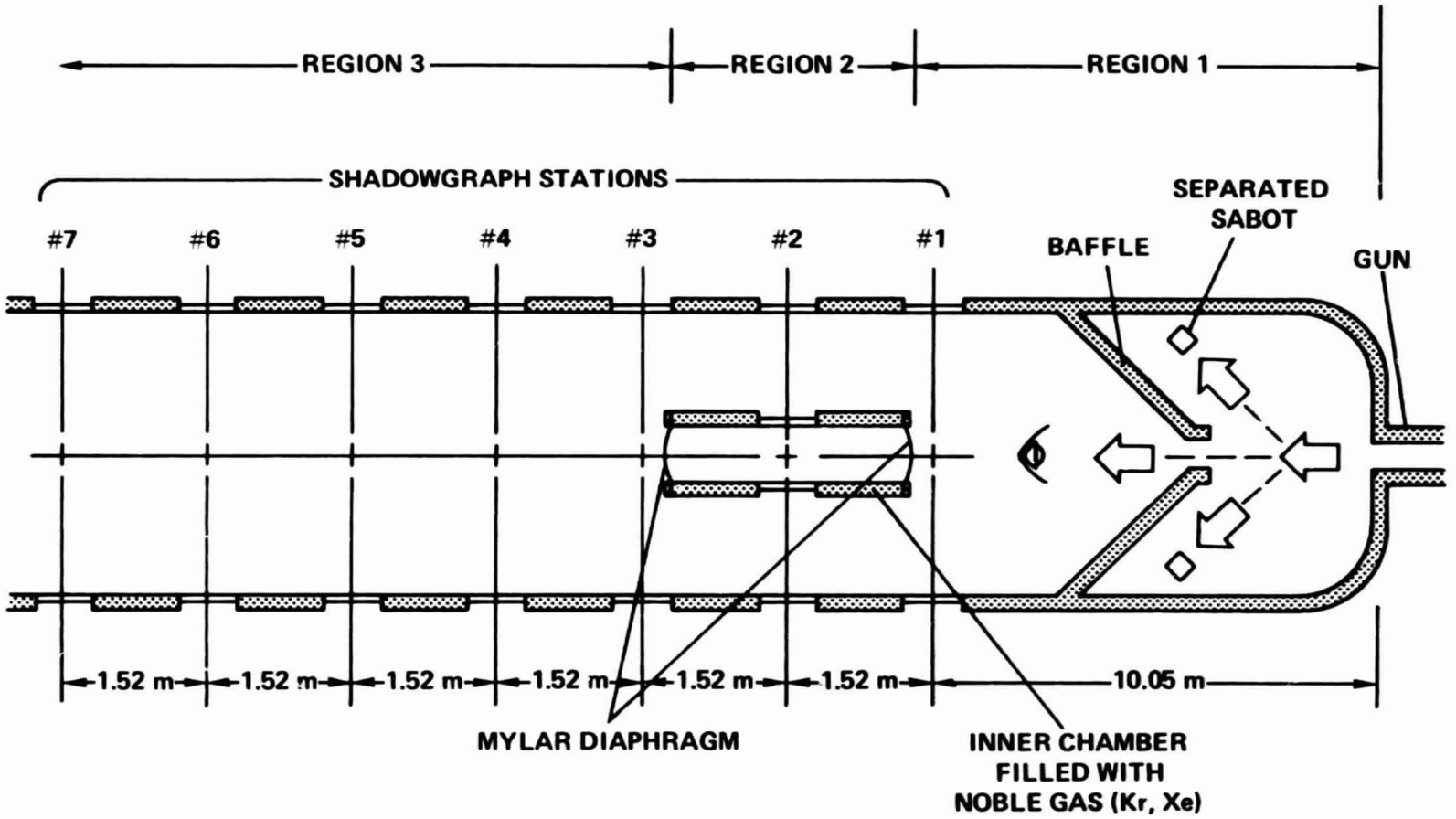

Figure 2.- Schematic of experimental setup.

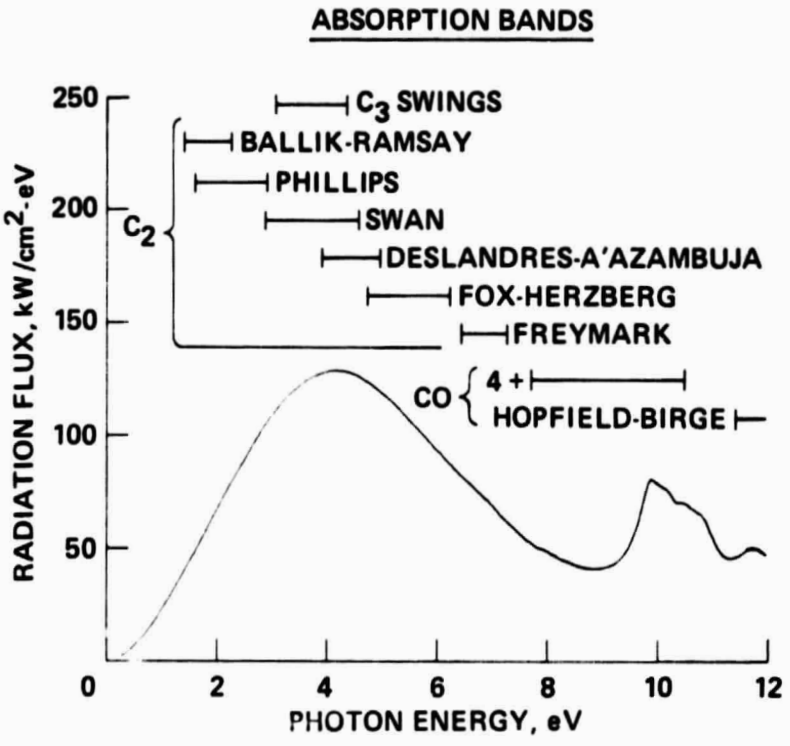

Figure 3.- Calculated spectra of unblocked stagnation-point radiative flux in krypton atmosphere. Free-stream pressure = 200 Torr; velocity = 4.5 km/sec; nose radius = 0.4763 cm (corresponding approximately to run 1542).

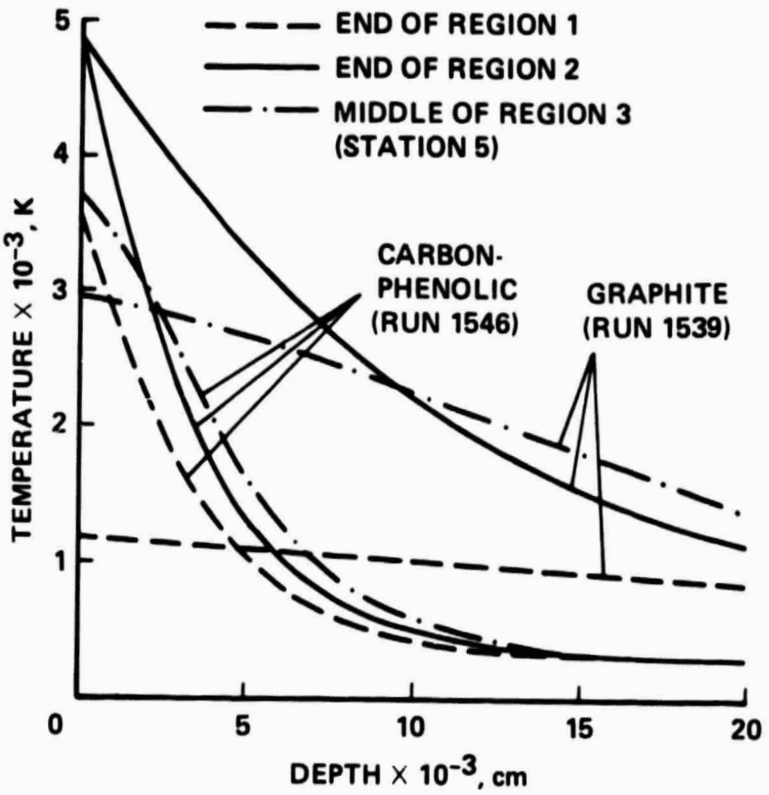

Figure 4.- Calculated temperature inside model at stagnation point.

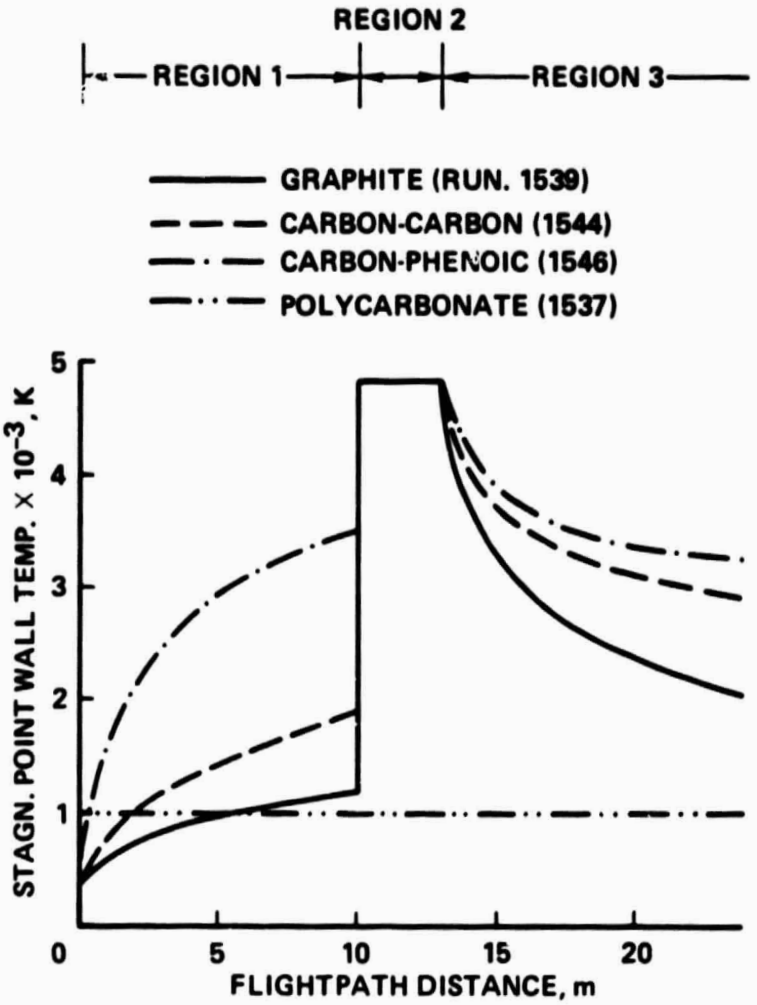

Figure 5.- Calculated wall temperature history at stagnation point.

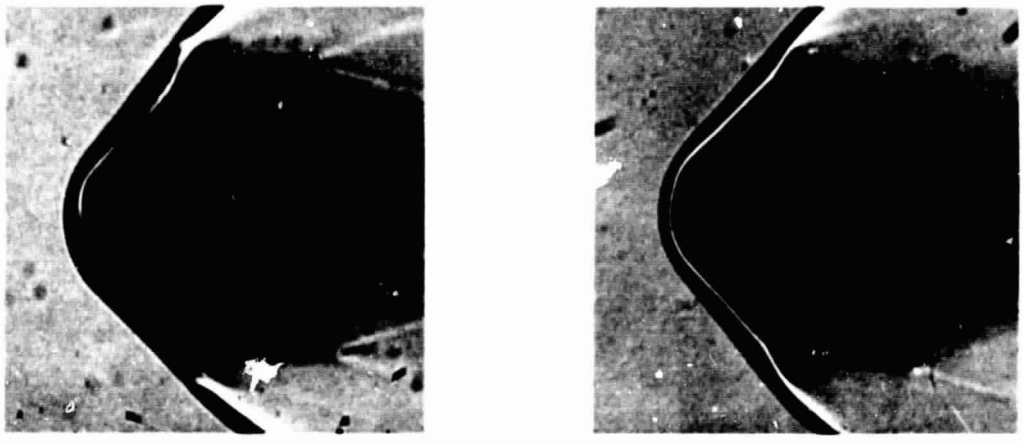

Figure 6.- Shadowgraphs for run 1536: polycarbonate model; q = 15.0 kW/cm^2 in region 1, 841 kW/cm^2 in region 2. (a) Station 1, side, (b) Station 5, side.

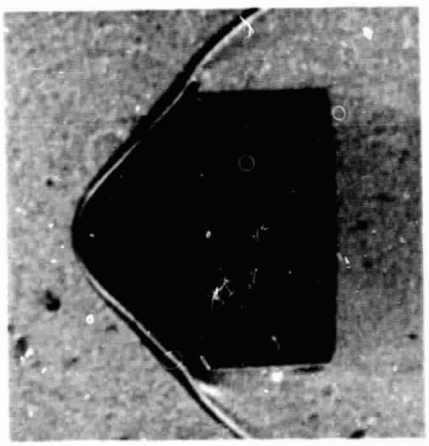

(a)

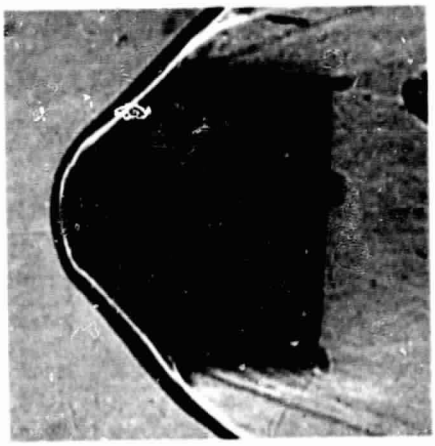

(b)

(c)

Figure 7.- Shadowgraphs for run 1537: polycarbonate model; q = 11.4 kW/cm^2 in region 1, 750 kW/cm^2 in region 2. (a) Station 1, top, (b) Station 5, side, (c) Station 2.

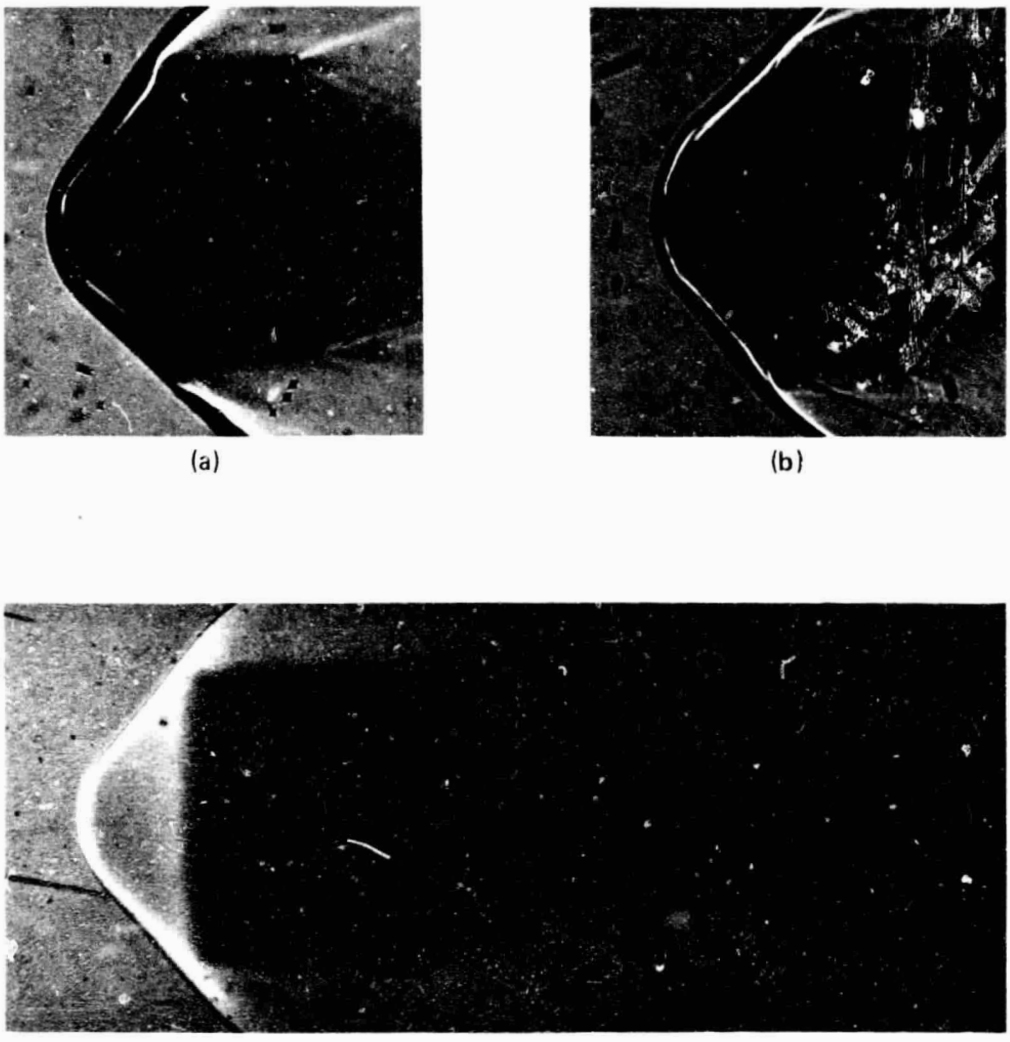

Figure 8.- Shadowgraphs for run 1538: polycarbonate model; q = 11.4 kW/cm^2 in region 1, 751 kW/cm^2 in region 2. (a) Station 1, side, (b) Station 5, side, (c) Station 2.

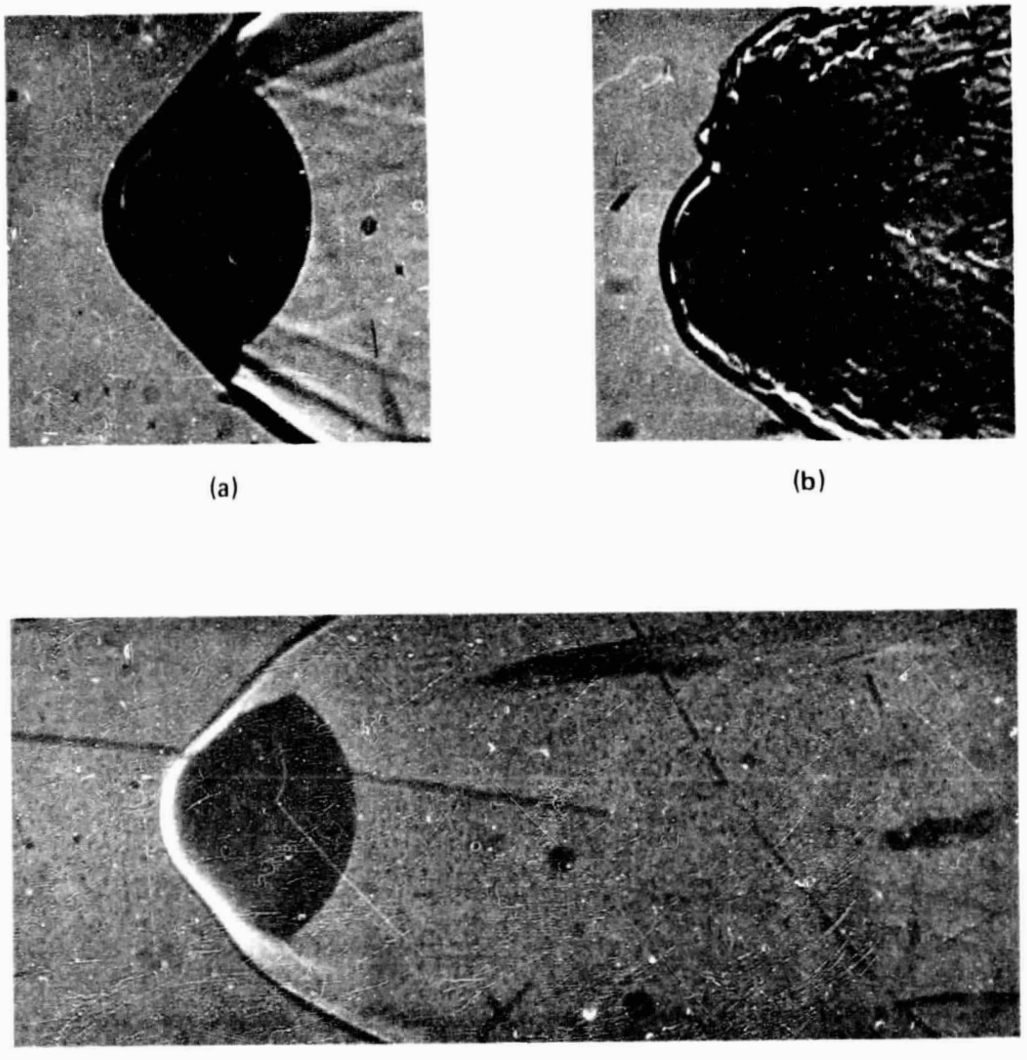

Figure 9.- Shadowgraphs for run 1539: AXF5Q graphite model; q = 13.9 kW/cm^2 in region 1, 755 kW/cm^2 in region 2. (a) Station 1, side, (b) Station 5, side, (c) Station 2.

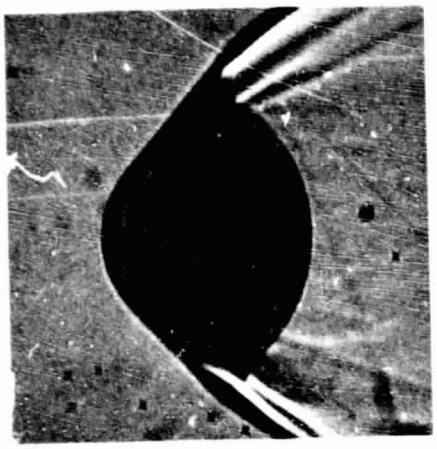

(a)

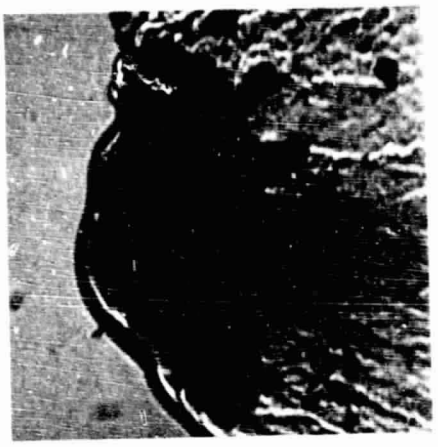

(b)

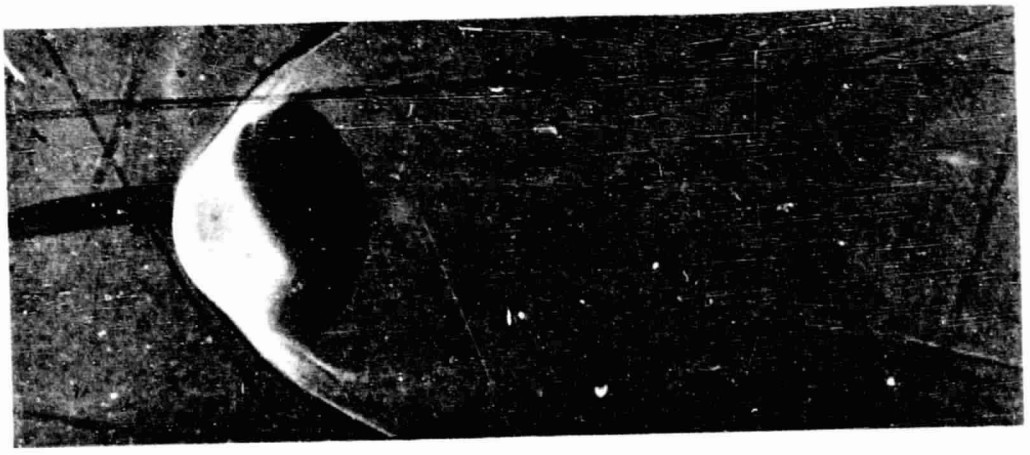

(c)

Figure 10.- Shadowgraphs for run 1540: AXF5Q graphite model; q = 13.7 kW/cm^2 in region 1, 832 kW/cm^2 in region 2. (a) Station 1, side, (b) Station 5, side, (c) Station 2.

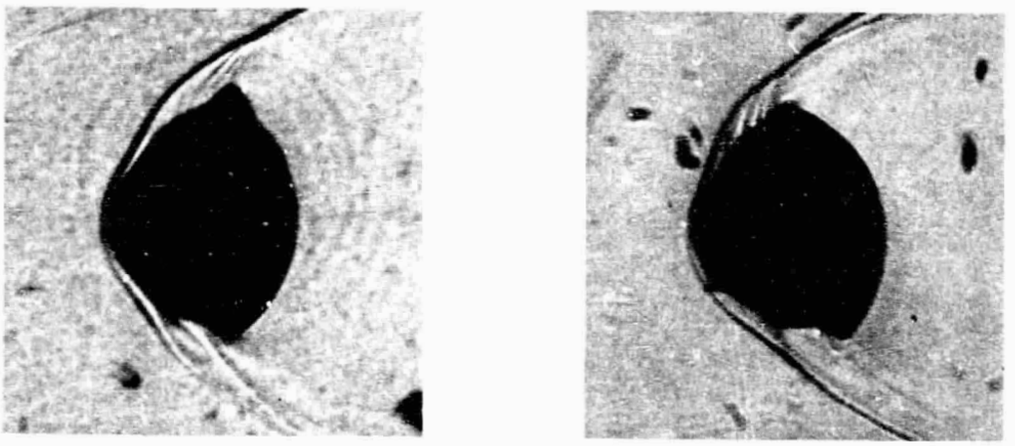

Figure 11.- Shadowgraphs for run 1541: AXF5Q graphite model; q = 10.0 kW/cm^2 in region 1, 832 kW/cm^2 in region 2. (a) Station 1, top, (b) Station 5, top.

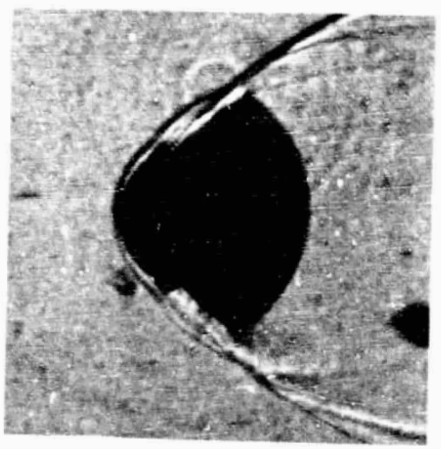

(a)

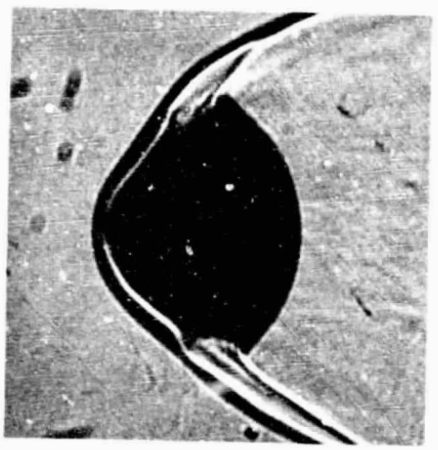

(b)

(c)

Figure 12.- Shadowgraphs for run 1542: AXF5Q graphite model; q = 16.4 kW/cm^2 in region 1, 1,000 kW/cm^2 in region 2. (a) Station 1, top, (b) Station 5, side, (c) Station 2.

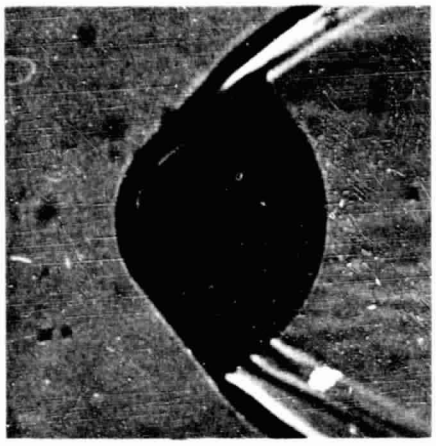

(a)

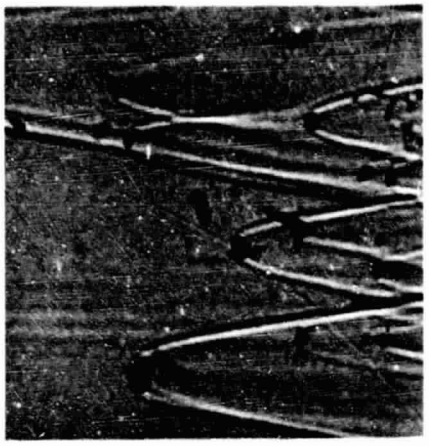

(b)

(c)

Figure 13.- Shadowgraphs for run 1543: AXF5Q graphite model; q = 15.9 kW/cm^2 in region 1, 1,150 kW/cm^2 in region 2. (a) Station 1, side, (b) Station 5, side, (c) Station 2.

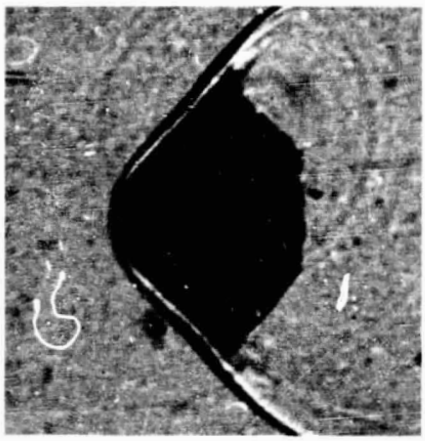

(a)

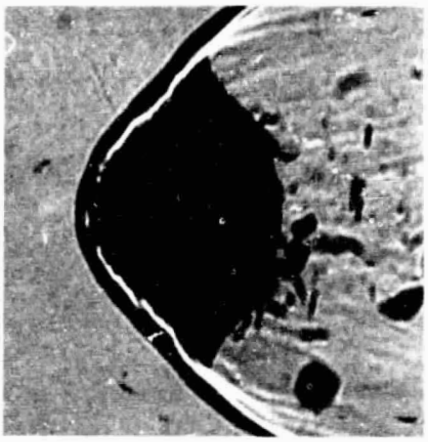

(b)

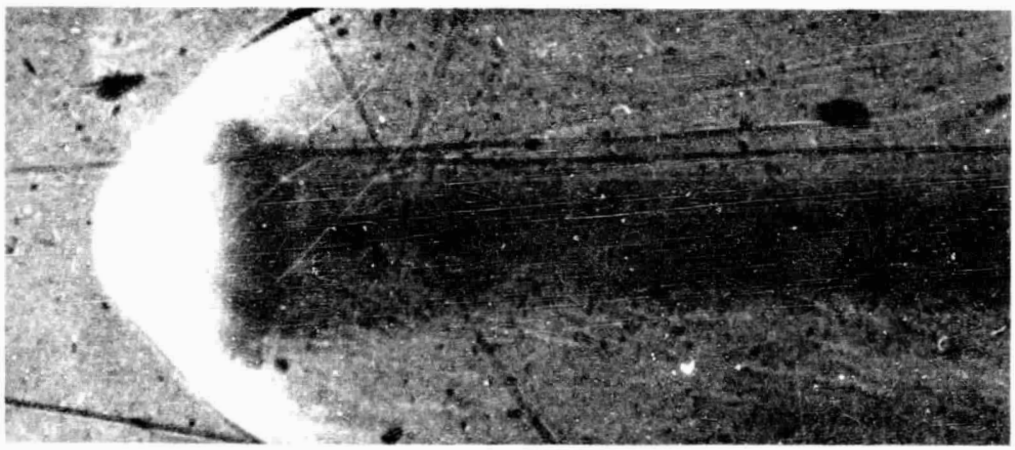

(c)

Figure 14.- Shadowgraphs for run 1544: carbon-carbon composite model; $q = 16.5$ kW/cm^2 in region 1, 1,260 kW/cm^2 in region 2. (a) Station 1, top, (b) Station 5, side, (c) Station 2.

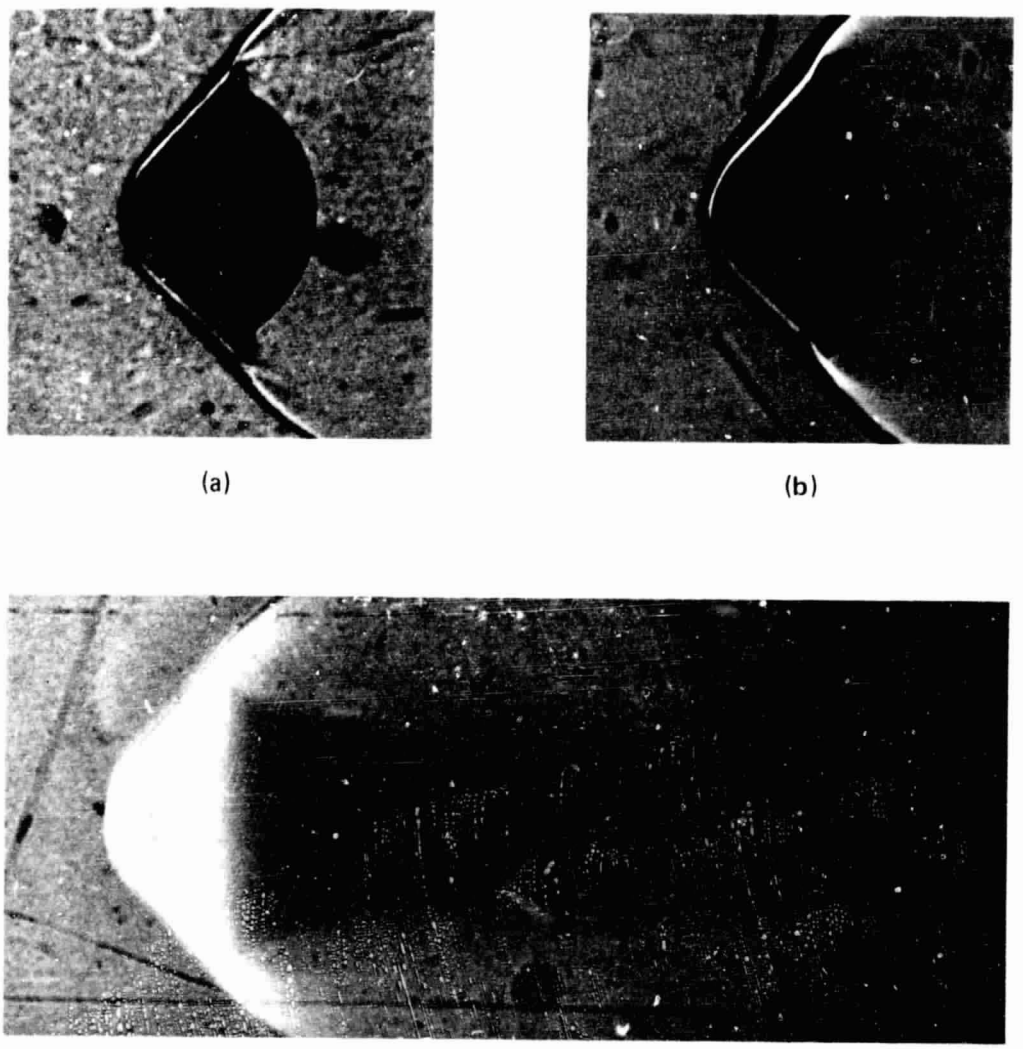

Figure 15.- Shadowgraphs for run 1545: carbon-phenolic model; q = 14.2 kW/cm^2 in region 1, 1,040 kW/cm^2 in region 2. (a) Station 1, top, (b) Station 7, side, (c) Station 2.

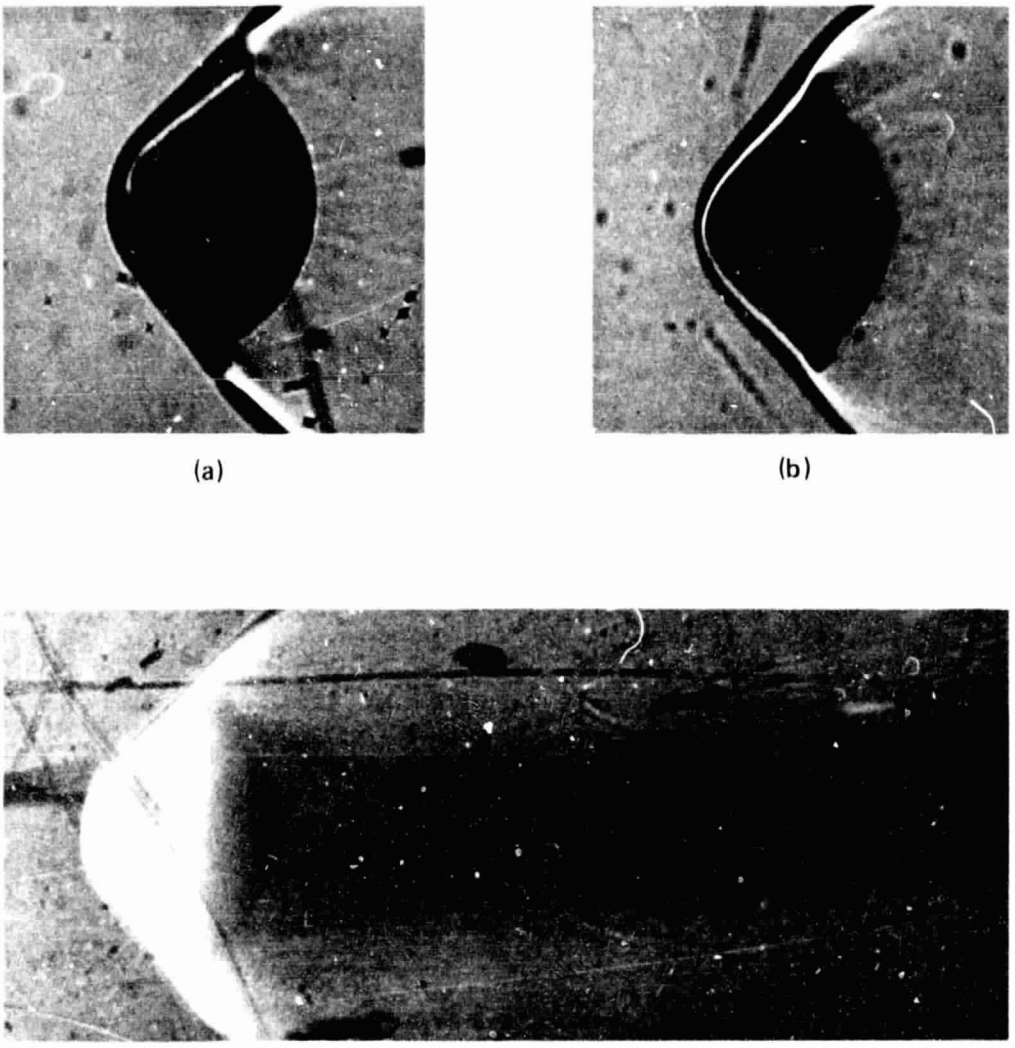

Figure 16.- Shadowgraphs for run 1546: carbon-phenolic model; q = 13.8 kW/cm^2 in region 1, 1,000 kW/cm^2 in region 2. (a) Station 1, side, (b) Station 7, side, (c) Station 2.

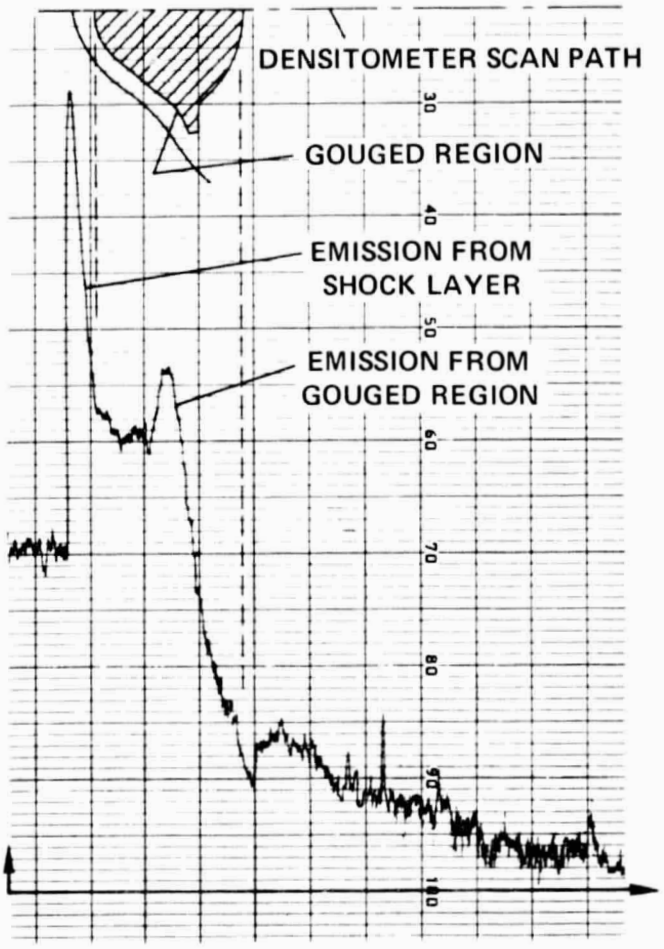

Figure 17.- Microphotodensitometer trace of shadowgraph at Station 2, carbon-phenolic model in xenon, run 1546, corresponding with figure 16(c).

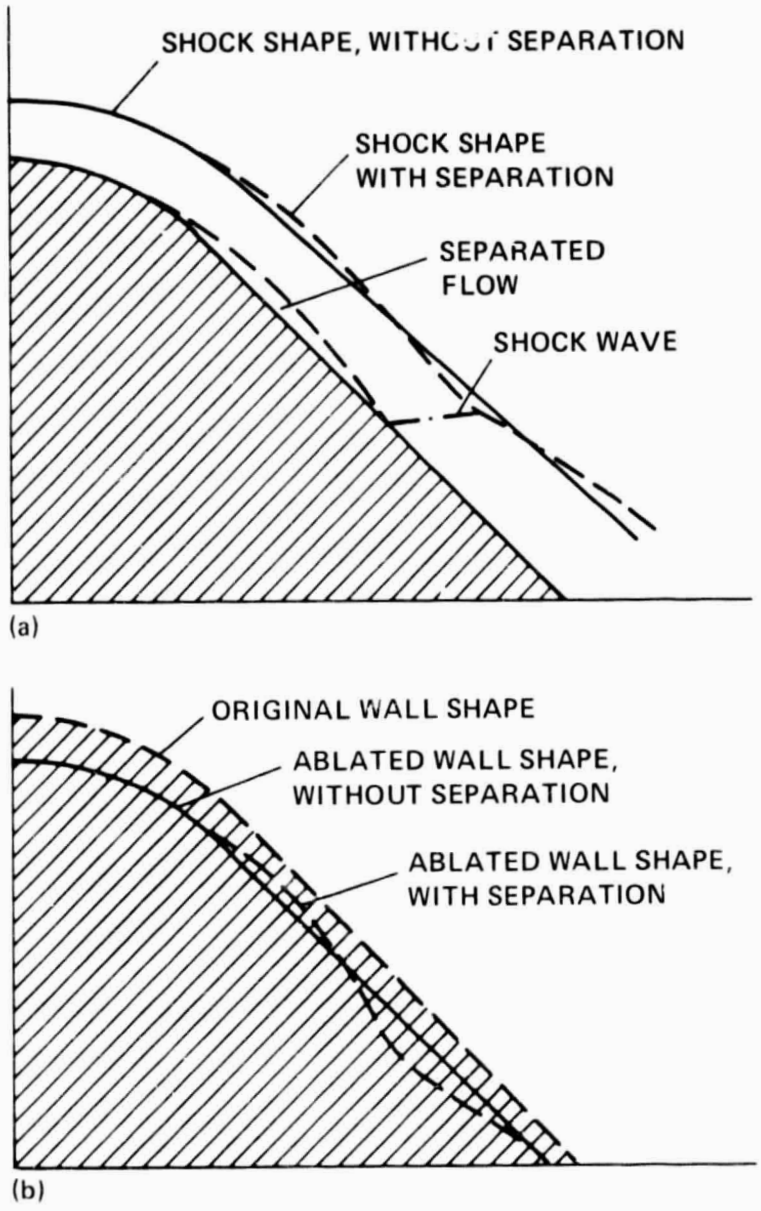

Figure 18.- Schematic comparison between the flow with and without separation. (a) Flow field, (b) Wall shape.

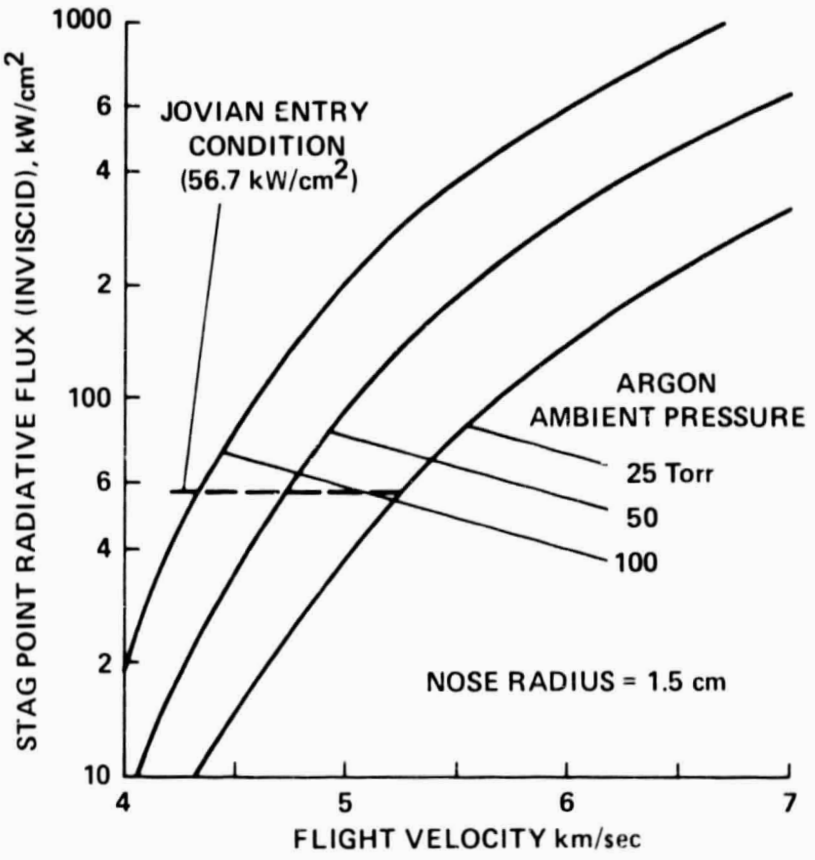

Figure 19.- Calculated radiative heat fluxes at stagnation point of an inviscid shock layer in argon, nose radius = 1.5 cm.

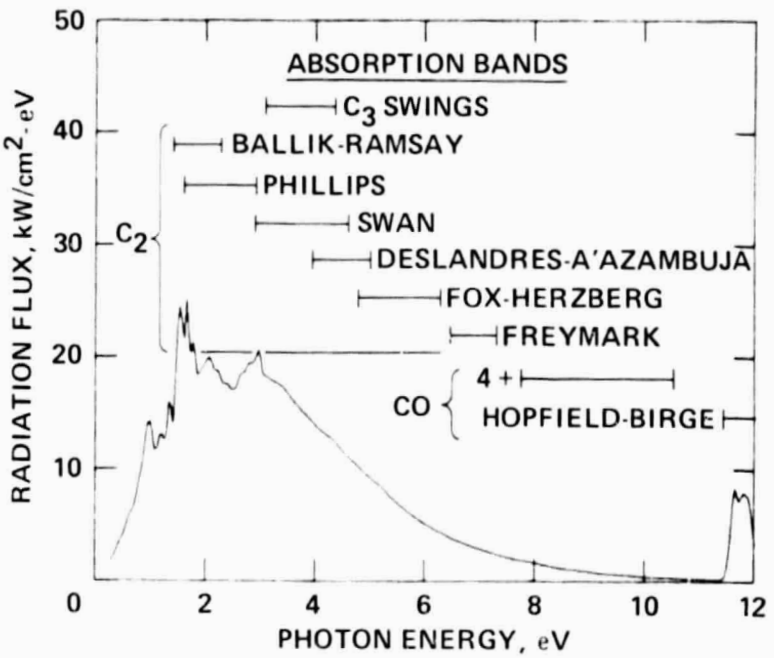

Figure 20.- Calculated spectra of unblocked stagnation-point radiative flux in argon atmosphere: free-stream pressure = 50 Torr; velocity = 5 km/sec; nose radius = 1.5 cm.